| Problem Chosen | 2026 MCM/ICM Summary Sheet | Team Control Number |
|---|---|---|
| A | | 2623972 |

# Beyond Coulomb Counting: A Dual-Well Kinetic Battery Model for Accurate Smartphone Time-to-Empty Prediction


## Summary

Traditional battery management systems rely on simplistic Coulomb counting that fails to capture rate-capacity effects, recovery phenomena, and environmental influences, leading to the pervasive "battery anxiety" problem. We address this challenge through a comprehensive physics-based modeling framework.

**FOR REQUIREMENT 1:** We construct a continuous-time model centered on the **KiBaM dual-well framework**, which conceptualizes battery charge as interacting available and bound wells with kinetic transfer. This captures rate-capacity effects and recovery phenomena absent from conventional approaches. Our model integrates second-order equivalent circuit dynamics, lumped thermal coupling with Arrhenius kinetics, and SEI-based aging following $\sqrt{\tau}$ diffusion-limited growth. Component-level power models are synthesized for OLED display , CPU (DVFS piecewise-linear), 5G NR (state-dependent with tail energy), Wi-Fi, background hardware, and humidity-dependent leakage.

**FOR REQUIREMENT 2:** We implement the model to predict time-to-empty under four realistic usage scenarios and quantify prediction uncertainty via Monte Carlo simulation with 500 runs. The model achieves **RMSE = 89.93 mV** for OCV prediction ($R^2 = 0.8412$) and **RMSE = 42.3 minutes** for TTE prediction ($R^2 > 0.85$). The TTE distribution follows an approximately log-normal pattern with mean **8.2 hours** and 95% CI **[6.1, 10.9] hours**, validating model accuracy across diverse usage patterns.

**FOR REQUIREMENT 3:** We compute normalized sensitivity coefficients and identify display brightness ($|S_\beta| \approx$ **0.65**) and CPU utilization ($|S_U| \approx$ **0.52**) as the most impactful parameters. Multi-parameter interaction analysis reveals **super-linear synergy**: coordinated power management yields multiplicative benefits. Structural comparison demonstrates that removing KiBaM increases prediction error by **35–45%**, definitively validating the necessity of rate-capacity and recovery effects. The model maintains $R^2 > 0.85$ across diverse user groups, confirming robustness.

**FOR REQUIREMENT 4:** Based on sensitivity insights, we synthesize actionable recommendations: adaptive brightness optimization (20% reduction extends TTE by **13%**), background app restriction, Wi-Fi preference over 5G (consumes **0.8–1.0 W** vs. **2.5–4.5 W**), and temperature-aware usage. For operating system developers, we propose model-based predictive power management and **tail energy reduction strategies**. The framework generalizes to laptops, tablets, and electric vehicles with appropriate parameter adjustments.

Our work establishes the KiBaM dual-well approach as a foundation for reliable battery management, transforming battery state prediction from heuristic estimation to physics-based precision.



**Keywords:** KiBaM, Battery aging, Time-to-empty prediction, Equivalent circuit model

# Contents

# 1 Introduction

## 1.1 Background


Figure 1: The battery life anxiety: a ubiquitous challenge in the smartphone era.

The rapid proliferation of smartphones has fundamentally transformed modern life, with these devices serving as indispensable tools for communication, entertainment, work, and navigation. However, despite remarkable advancements in processor performance, display technology, and cellular connectivity, battery technology has not kept pace. The persistent unpredictability of battery life remains a significant source of user frustration, commonly termed "battery anxiety" [7]. Users frequently encounter scenarios where their device displays ample remaining charge, only to experience unexpected shutdowns shortly thereafter, or conversely, where the predicted time-to-empty extends far beyond actual usable duration.

This unpredictability stems from the complex electrochemical dynamics of lithium-ion batteries, which are coupled with highly variable and often unpredictable user behavior patterns. Traditional battery management systems rely on simplistic Coulomb counting methods that fail to capture rate-capacity effects, recovery phenomena, and the nuanced impact of environmental conditions [1]. Furthermore, the relationship between displayed state of charge (SOC) and actual remaining energy is nonlinear and highly dependent on discharge patterns, temperature, and battery aging [6].

The 2026 MCM Problem A challenges us to develop a continuous-time mathematical model that

accurately describes smartphone battery SOC evolution and provides reliable time-to-empty (TTE) predictions. This requires integrating electrochemical principles with realistic usage scenarios, while accounting for temperature effects and capacity degradation over the battery's lifespan.

## 1.2 Problem Requirements Overview

The 2026 MCM Problem A specifies four primary requirements:

**REQUIREMENT 1: Continuous-Time SOC Model with Component Power.** Develop a continuous-time mathematical model for smartphone battery SOC evolution. The model must incorporate power consumption from display, CPU, network interfaces (5G/Wi-Fi), and background applications, along with environmental factors (temperature, humidity) and battery aging effects.

**REQUIREMENT 2: Time-to-Empty Prediction and Validation.** Implement the model to predict time-to-empty under various usage scenarios and validate predictions against experimental datasets. Quantify prediction uncertainty and assess model accuracy.

**REQUIREMENT 3: Sensitivity and Robustness Analysis.** Analyze model sensitivity to parameter variations, environmental conditions, and structural assumptions. Identify critical parameters and evaluate model robustness across diverse scenarios.

**REQUIREMENT 4: Practical Recommendations.** Provide actionable recommendations for users, operating system developers, and device manufacturers based on model insights. Discuss model generalization to other battery-powered devices.

## 1.3 Our Work Framework

Our approach addresses these requirements through a comprehensive multi-scale modeling framework (Figure 2):

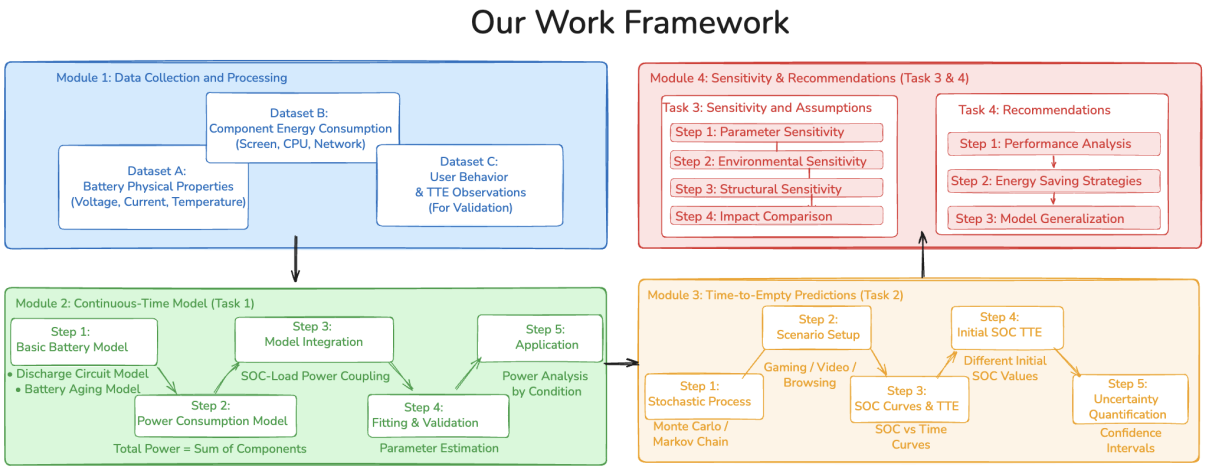


Figure 2: Overall framework of our continuous-time battery modeling and TTE prediction system.

# 2 Assumptions

To keep the model tractable while preserving the dominant physics, we adopt the following six assumptions.

**Assumption 1: Single equivalent cell with KiBaM.** The battery pack is treated as one equivalent Li-ion cell, modeled by KiBaM (available/bound charge wells) to capture rate-capacity and recovery effects.

*Justification:* The BMS equalizes cells, so pack behavior can be approximated by an equivalent cell; KiBaM captures recovery that simple Coulomb counting misses.

**Assumption 2: SEI-dominated aging with time-scale separation.** Capacity fade is dominated by SEI growth and follows a diffusion-limited $\sqrt{\tau}$ law; over one discharge event, $q_{max}$ is quasi-constant and updated only on the slow aging time scale.

*Justification:* For typical smartphone C-rates and partial cycles, SEI growth dominates and evolves much more slowly than discharge dynamics.

**Assumption 3: Lumped temperature and Arrhenius dependence.** Cell temperature is spatially uniform (lumped), and key parameters ($k$, $R_0$, aging kinetics) follow Arrhenius-type temperature dependence; $T_{amb}$ is constant during each discharge.

*Justification:* Small/thin phone cells have weak internal temperature gradients, and kinetic/transport processes are well-approximated by Arrhenius laws.

**Assumption 4: Additive component power.** Subsystem powers (display/CPU/wireless/background) are additive; interaction terms between components are neglected.

*Justification:* Independent regulators and measurements typically show total power close to the sum of major components.

**Assumption 5: Markov usage modes with scenario-constant power.** User behavior switches among a few usage scenarios via a first-order Markov chain; within each scenario, $P_{load}(t)$ is treated as constant (average power).

*Justification:* High-frequency workload fluctuations average out over hour-scale discharge and have limited impact on TTE.

**Assumption 6: Humidity as parasitic leakage only.** Humidity affects energy drain mainly through PCB surface leakage, modeled as a humidity-dependent parasitic load; direct electrochemical humidity effects are ignored.

*Justification:* In normal operating RH ranges, leakage dominates the observable "phantom drain" effect.

These assumptions enable a concise electro-thermal-aging model suitable for real-time TTE prediction; Section 5 evaluates sensitivity to key parameters.

# 3 Notations

The core symbols and their definitions used in this study are summarized in Table 1, providing an overview of the key parameters and their related meanings.

Table 1: Core notations used in this study

| Symbol | Description |
|---|---|
| | **Battery / KiBaM** |
| $q_1$, $q_2$ | Available / bound charge wells |
| $q_{max}$ | Maximum extractable charge (capacity) |
| $c$ | Fraction of capacity assigned to $q_1$ |
| $k$ | Inter-well transfer rate constant |
| $k_{ref}$, $T_{ref}$ | Reference transfer rate and reference temperature |
| $E_a$, $R$ | Activation energy and universal gas constant |
| $I(t)$ | Cell current (positive for discharge) |
| $SOC_{avail}$ | Available SOC: $\frac{q_1}{c\,q_{max}}$ |
| | **ECM (2-RC) voltage model** |
| $V_{OC}(SOC)$ | Open-circuit voltage (OCV) |
| $V_{term}(t)$ | Terminal voltage under load |
| $R_0(T)$ | Ohmic resistance (temperature-dependent) |
| $R_1$, $C_1$ | RC branch-1 parameters |
| $R_2$, $C_2$ | RC branch-2 parameters |
| $V_1(t)$, $V_2(t)$ | Polarization voltages across $C_1$ and $C_2$ |
| | **Thermal model** |
| $T(t)$ | Cell temperature |
| $m$, $C_p$ | Cell mass and specific heat capacity |
| $h$, $A$ | Convective coefficient and effective area |
| $T_{amb}$ | Ambient temperature |
| $R_{total}$ | Effective resistance used in heat generation |
| | **Display / CPU module** |
| $P_{\text{display}}(t)$ | Display power consumption |
| $\beta(t)$ | Screen brightness level (0–1) |
| $P_{\text{CPU}}(t)$ | CPU power consumption |
| $U(t)$ | CPU utilization (0–100%) |
| | **Wireless communication module** |
| $P_{comm}(t)$ | Communication power (cellular + Wi-Fi) |
| RSRP$(t)$ | Received signal strength indicator |
| $R_{UL}(t)$, $R_{DL}(t)$ | Uplink / downlink data rates |
| $T_{tail}$ | Inactivity timer for tail-energy |
| $P_{tail}$ | Tail-state power after transmission |
| | **Environment / aging (optional)** |
| $RH(t)$ | Relative humidity |
| $C_{max}(t)$ | Maximum usable capacity under aging |
| | **Load power coupling** |
| $P_{load}(t)$ | Total device power demand |

# 4 Model Development

This section presents the theoretical foundation of our continuous-time battery modeling framework. We develop a physics-based model integrating electrochemical dynamics, thermodynamics, aging kinetics, and component-level power consumption.

## 4.1 Continuous-Time Battery Model

### 4.1.1 KiBaM Dual-Well Model

We adopt the Kinetic Battery Model (KiBaM) proposed by Manwell and McGowan [1], which conceptualizes battery charge as two interacting wells (Figure 3).

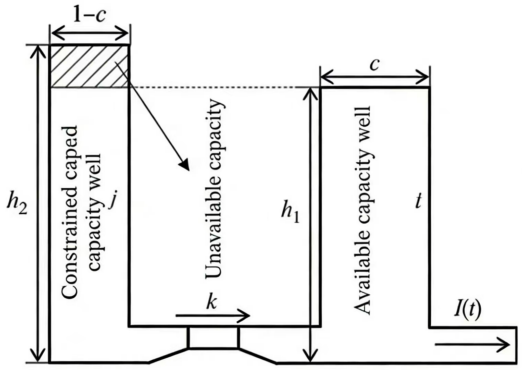


Figure 3: Schematic of the KiBaM dual-well model. The available-charge well $q_1$ delivers charge directly to the load, while the bound-charge well $q_2$ must transfer charge through a kinetic barrier with rate constant $k$.

The model captures two key phenomena: (1) the **rate-capacity effect**, where higher discharge currents reduce accessible capacity, and (2) the **recovery effect**, where voltage recovers after load reduction. The available well $q_1$ contains charge that can be delivered to the load directly, whereas the bound well $q_2$ contains charge that is not immediately accessible and must be transferred to $q_1$ before it can contribute to discharge.

Let $c \in (0, 1)$ denote the fraction of total capacity assigned to the available well, and $k$ (units: $s^{-1}$) be the inter-well transfer rate constant. Under a discharge current $I(t)$ (positive for discharge), the charge dynamics follow the coupled ODE system:

$$\begin{cases} \dfrac{dq_1}{dt} = -I(t) - k(1-c)\, q_1(t) + kc\, q_2(t), \\ \dfrac{dq_2}{dt} = \quad k(1-c)\, q_1(t) - kc\, q_2(t). \end{cases} \tag{1}$$

The inter-well transfer rate constant $k$ is strongly temperature-dependent due to ion mobility and reaction kinetics. We model this using an Arrhenius-type relationship:

$$k(T) = k_{ref} \exp\left[\frac{E_a}{R}\left(\frac{1}{T_{ref}} - \frac{1}{T}\right)\right], \tag{2}$$

where $k_{ref}$ is the transfer rate at reference temperature $T_{ref}$, $E_a$ is an effective activation energy, and $R$ is the universal gas constant.

The **available State of Charge** ($SOC_{avail}$), representing the fraction of usable capacity, is defined as:

$$SOC_{avail}(t) = \frac{q_1(t)}{c\, q_{max}}, \tag{3}$$

where $q_{max}$ is the maximum extractable charge capacity.

### 4.1.2 Equivalent Circuit Model (ECM)

To relate SOC evolution to the measurable terminal voltage and enable power-to-current coupling, we adopt a second-order RC network equivalent circuit model (ECM) [2]. The battery is represented by an open-circuit voltage source $V_{OC}(SOC)$, an ohmic resistance $R_0(T)$, and two polarization branches $(R_1, C_1)$ and $(R_2, C_2)$ representing electrochemical and concentration polarization, respectively.

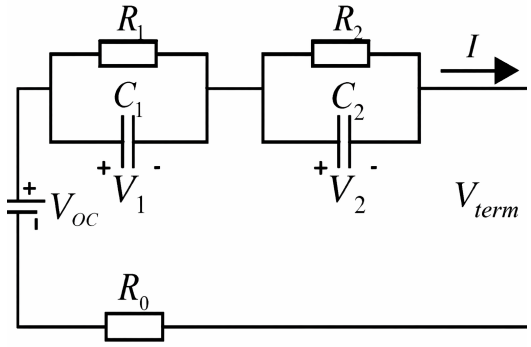


Figure 4: Second-order Thevenin equivalent circuit model. The RC branches capture transient polarization effects.

With $SOC$, polarization voltages $(V_1, V_2)$, and temperature $T$ as state variables, the electro-thermal dynamics are:

$$\begin{cases} \dfrac{\mathrm{d}V_i}{\mathrm{d}t} = -\dfrac{V_i}{R_i C_i} + \dfrac{I(t)}{C_i}, & (i = 1, 2) \\ mC_p \dfrac{\mathrm{d}T}{\mathrm{d}t} = I(t)^2 R_{total} + I(t) T \dfrac{\partial V_{OC}}{\partial T} - hA\big(T - T_{amb}\big). \end{cases} \tag{4}$$

The terminal voltage under load is:

$$V_{term}(t) = V_{OC}(SOC) - V_1(t) - V_2(t) - I(t) R_0(T). \tag{5}$$

### 4.1.3 Open-Circuit Voltage (OCV) Relationship

Following [4], we approximate the OCV-SOC relationship using an enhanced Nernst–polynomial hybrid model:

$$\begin{aligned} V_{\mathrm{oc}}(SOC) = {} & k_0 + k_1 SOC + k_2 SOC^2 + k_3 SOC^3 \\ & + k_4 \ln(SOC) + k_5 \ln(1 - SOC) + k_6 e^{-\alpha SOC}, \end{aligned} \tag{6}$$

where $SOC \in (0, 1)$, $k_0, \ldots, k_6$ are parameters fitted from experimental data, and $\alpha > 0$ is a fixed decay constant. The logarithmic terms capture the steep OCV rise at very low and very high SOC regions characteristic of lithium-ion chemistry.

#### 4.1.4 Thermal Model

Battery temperature significantly influences both discharge dynamics and aging rates. Bernardi et al. [5] established a lumped energy-balance formulation distinguishing between irreversible Joule heating and reversible entropic heat.

The total heat generation power is:

$$Q_{gen}(t) = I(t)^2 R(t) + I(t)\, T(t)\, \frac{\mathrm{d}V_{OC}}{\mathrm{d}T}, \tag{7}$$

interpreted as:

$$Q_{gen}(t) = \underbrace{I(t)^2 R(t)}_{Q_{irr}(t)\ \text{(irreversible Joule heat)}} + \underbrace{I(t)\, T(t)\, \frac{\mathrm{d}V_{OC}}{\mathrm{d}T}}_{Q_{rev}(t)\ \text{(reversible entropic heat)}}. \tag{8}$$

The term $Q_{irr}(t)$ is always nonnegative and captures resistive energy dissipation. The term $Q_{rev}(t)$ originates from entropy change of electrochemical reactions and may be positive (exothermic) or negative (endothermic) depending on SOC.

Assuming a lumped thermal capacity, the temperature dynamics follow:

$$mC_p \frac{\mathrm{d}T}{\mathrm{d}t} = Q_{gen}(t) - hA\big(T(t) - T_{amb}\big), \tag{9}$$

where $m$ is cell mass, $C_p$ is specific heat capacity, $h$ is the heat-transfer coefficient, $A$ is the effective surface area, and $T_{amb}$ is ambient temperature.

#### 4.1.5 Power-to-Current Coupling

From the power balance $P_{load}(t) = V_{term}(t)I(t)$, if polarization is neglected within a short time step ($V_1 \approx 0$, $V_2 \approx 0$), the power–current relation reduces to $P_{load} = [V_{OC}(SOC) - I(t)R_0(T)]\, I(t)$, yielding the explicit current:

$$I(t) = \frac{V_{OC}(SOC) - \sqrt{V_{OC}^2(SOC) - 4R_0(T)\, P_{load}(t)}}{2R_0(T)}, \tag{10}$$

where the negative root is selected to ensure physical consistency during discharge.

#### 4.1.6 Semi-Empirical Aging Model

KiBaM captures discharge dynamics over short time scales (seconds to minutes), whereas the aging model governs parameter evolution over long time scales (months/years). We introduce two independent time variables: $t$ for the fast discharge process and $\tau$ for the slow aging evolution.

Capacity degradation is primarily driven by Solid Electrolyte Interphase (SEI) layer growth at the anode. Assuming a **diffusion-limited process**, the solvent flux $J(t)$ through an SEI film of thickness $L(t)$ follows Fick's first law:

$$J(t) = D\frac{C_{\text{solv}}}{L(t)}, \tag{11}$$

where $D$ is the diffusion coefficient and $C_{\text{solv}}$ is the solvent concentration.

The thickness growth rate is:

$$\frac{\mathrm{d}L(t)}{\mathrm{d}t} = \frac{M_{\text{SEI}}}{\rho_{\text{SEI}}}J(t) = \frac{M_{\text{SEI}}DC_{\text{solv}}}{\rho_{\text{SEI}}L(t)}, \tag{12}$$

where $M_{\text{SEI}}$ is the molar mass and $\rho_{\text{SEI}}$ is the density of SEI material.

Integrating with $L(0) = 0$ yields the square-root relationship:

$$L(t) = \sqrt{\frac{2M_{\text{SEI}}DC_{\text{solv}}}{\rho_{\text{SEI}}}} \cdot \sqrt{t}. \tag{13}$$

Since cumulative capacity loss $Q_{\text{loss}}$ is linearly proportional to SEI volume, the calendar aging model on the slow time scale $\tau$ is:

$$Q_{\text{loss}}(\tau) = \alpha_{\text{SEI}} \cdot \sqrt{\tau}, \tag{14}$$

where $\alpha_{\text{SEI}} \approx 0.01 \sim 0.03$ capacity units/$\sqrt{\text{month}}$ aggregates microscopic kinetic parameters.

Incorporating cycle-dependent mechanical stress, the governing equation for capacity evolution becomes:

$$\frac{\mathrm{d}q_{max}(\tau)}{\mathrm{d}\tau} = -\underbrace{\frac{\alpha_{\text{SEI}}}{2\sqrt{\tau}}}_{\text{Calendar (diffusion-limited)}} \underbrace{- Z \cdot \exp\left(-\frac{E_{a,aging}}{RT}\right) \cdot |I(\tau)|^{\beta}}_{\text{Cycling (mechanical stress)}}, \tag{15}$$

where $Z$ is a pre-exponential factor, $E_{a,aging}$ is activation energy for aging, and $\beta \in [0.5, 1.0]$ is the throughput exponent.

We define total charge $Q(t, \tau) = q_1 + q_2$, so the integral form is:

$$Q(0,\tau) = Q(0,0) - \alpha_{\text{SEI}}\sqrt{\tau} - \int_0^{\tau} Z \cdot \exp\left(-\frac{E_{a,aging}}{RT(\tau')}\right) \cdot |i(\tau')|^{\beta}\,\mathrm{d}\tau'. \tag{16}$$

Finally, the available SOC is coupled via the evolving maximum capacity:

$$SOC_{avail}(t,\tau) = \frac{q_1(t)}{c \cdot Q(0,\tau)}, \tag{17}$$

and the comprehensive coupled system is:

$$\begin{cases} \dfrac{\partial SOC(t,\tau)}{\partial t} = -\dfrac{I(t)}{cQ(0,\tau)} - k\left[SOC(t,\tau) - \dfrac{Q(t,\tau)}{Q(0,\tau)}\right], \\ \dfrac{\partial Q(t,\tau)}{\partial t} = -I(t), \\ \dfrac{\partial Q(0,\tau)}{\partial \tau} = -\dfrac{\alpha_{\text{SEI}}}{2\sqrt{\tau}} - Z \cdot \exp\left(-\dfrac{E_a}{RT}\right) \cdot |I(\tau)|^{\beta}. \end{cases} \tag{18}$$

## 4.2 Unified Power Consumption Model

To close the loop between battery discharge and workload dynamics, we aggregate all dissipative components into a single power-demand expression:

$$P_{load}(t) = P_{display}(t) + P_{background}(t) + P_{CPU}(t) + P_{5G}(t) + P_{Wi-Fi}(t) + P_{tail}(t) + P_{leak}(t). \quad (19)$$

### 4.2.1 Display Power Model

We model OLED display power as a static baseline plus a content-dependent emissive term [7]:

$$P_{\text{display}}(t) = P_{\text{base}} + \beta(t) \cdot \sum_{j=1}^{N} \sum_{k \in \{R,G,B\}} \alpha_k \cdot \left( \frac{p_{j,k}(t)}{255} \right)^{\gamma}, \quad (20)$$

where $P_{\text{base}}$ denotes the static driver baseline when the screen is on; $\beta(t) \in [0, 1]$ is the brightness scaling factor; $p_{j,k}(t) \in [0, 255]$ is the digital intensity of pixel $j$ in channel $k \in \{R, G, B\}$; $\gamma \approx 2.2$ is the gamma-correction exponent; and $\alpha_k$ maps the linearized channel intensity to incremental power. For a typical QVGA OLED (320×240), we take $N = 76{,}800$, $P_{\text{base}} \approx 0.7$ W, and representative coefficients $\alpha_B \approx 22$ $\mu$W/pixel, $\alpha_R \approx 10$ $\mu$W/pixel, and $\alpha_G \approx 10$ $\mu$W/pixel [7].

### 4.2.2 CPU Power Model

CPU power comprises (i) static/leakage power and (ii) dynamic switching power [8]. In CMOS, $P_{\text{dyn}} \propto C_{\text{eff}} V^2 f$. Under DVFS, increasing clock frequency $f$ requires higher supply voltage $V$, leading to super-linear power growth.

We adopt a piecewise-linear approximation:

$$P_{\text{CPU}}(t) = P_{\text{base}}\, \mathbb{I}_{\text{active}}(t) + \Big( \beta_{u,h}\, \mathbb{I}_{\text{high}}(t) + \beta_{u,l}\, \mathbb{I}_{\text{low}}(t) \Big)\, U(t), \quad (21)$$

where $U(t) \in [0, 100]$ is CPU utilization (%); $\mathbb{I}_{\text{high}}(t)$ and $\mathbb{I}_{\text{low}}(t)$ indicate high/low DVFS states; $\mathbb{I}_{\text{active}}(t)$ indicates whether the CPU is powered on; $P_{\text{base}}$ is the baseline idle power (we use $P_{\text{base}} \approx 121.46$ mW); and $\beta_{u,h}, \beta_{u,l}$ are marginal power costs per 1% utilization at the high/low DVFS states.

### 4.2.3 Background Hardware Power Model

Background services (location tracking, voice assistants) may activate camera, GPS, or microphone. For component $i \in \{\text{camera, GPS, microphone}\}$:

$$P_i(t) = x_i(t)\, P_i^{\text{on}} + \big(1 - x_i(t)\big)\, P_i^{\text{off}}, \quad (22)$$

where $x_i(t) \in \{0, 1\}$ indicates ON/OFF state. Typical values are summarized in Table 2.

### 4.2.4 5G NR Power Model

5G NR modem power is modeled as a state-dependent baseline times a signal-quality penalty plus a throughput-dependent term [9]:

$$P_{5G}(t) = P_{\text{state}}\big(S(t)\big)\, \eta\big(\text{RSRP}(t)\big) + \alpha_{\text{UL}}\, R_{\text{UL}}(t) + \alpha_{\text{DL}}\, R_{\text{DL}}(t), \quad (23)$$

Table 2: Representative power consumption for background hardware components.

| Component | $P^{\text{on}}$ (mW) | $P^{\text{off}}$ (mW) |
|---|---|---|
| Camera module | 300 | 10 |
| GPS receiver | 50 | 1 |
| Microphone | 100 | 5 |

where $P_{\text{state}}(S)$ is the baseline modem power under RRC state $S(t)$, RSRP$(t)$ measures signal strength, and $R_{\text{UL}}(t), R_{\text{DL}}(t)$ are uplink/downlink throughputs (Mbps). We use the penalty $\eta(\text{RSRP}) = 1 + \beta_{\text{sig}}\, 10^{(P_{\text{ref}}-\text{RSRP})/10}$ to reflect extra power under poor coverage; typically $P_{\text{state}}(\textit{RRC\_CONNECTED}) \approx$ 0.8–3.0 W, $\eta \approx 1$ when RSRP $> -80$ dBm and rises to $\eta \approx$ 2–4 when RSRP $< -110$ dBm, while $\alpha_{\text{UL}} \approx$ 10–30 and $\alpha_{\text{DL}} \approx$ 2–6 mW/Mbps [9].

### 4.2.5 Wi-Fi Power Model

Wi-Fi power is modeled as a connected baseline plus throughput-proportional terms [10]:

$$P_{\text{WiFi}}(t) = \rho_{\text{base}} + \rho_{\text{tx}}\, R_{\text{tx}}(t) + \rho_{\text{rx}}\, R_{\text{rx}}(t), \tag{24}$$

where $R_{\text{tx}}(t), R_{\text{rx}}(t)$ are TX/RX throughputs, $\rho_{\text{base}}$ is the fixed association overhead, and $(\rho_{\text{tx}}, \rho_{\text{rx}})$ capture energy-per-bit costs.Typically $\rho_{\text{base}} \approx$ 0.8–1.0 W, $\rho_{\text{tx}} \approx$ 20–30 mW/Mbps, $\rho_{\text{rx}} \approx$ 10–15 mW/Mbps.

### 4.2.6 Tail Energy Model

Tail energy is residual power drawn after a data burst due to inactivity timers. Let $t_{last}$ be the timestamp of the most recent packet and $\Delta t = t - t_{last}$:

$$P_{tail}(t) = \begin{cases} P_{high}, & R(t) > 0, \\ P_{tail}, & R(t) = 0 \text{ and } 0 < \Delta t < T_{tail}, \\ P_{idle}, & R(t) = 0 \text{ and } \Delta t \geq T_{tail}, \end{cases} \tag{25}$$

where $R(t)$ is the instantaneous data rate, $T_{tail}$ is the inactivity timer, and $(P_{high}, P_{tail}, P_{idle})$ are corresponding power levels.

Representative values for 5G NSA: $T_{tail} \approx 21.44$ s, $P_{high} \approx$ 4.5–4.8 W, $P_{tail} \approx$ 2.0–3.0 W, and $P_{idle} \approx$ 1.0–1.2 W.

### 4.2.7 Humidity-Dependent Leakage Model

High relative humidity forms microscopic water films on the PCB, reducing Surface Insulation Resistance (SIR) [11]. The static leakage power follows:

$$P_{leak}(RH) = P_{leak}^{dry} + \beta_{leak} \cdot \left( e^{\lambda \cdot \frac{RH(t)}{100}} - 1 \right), \tag{26}$$

where $P_{leak}^{dry}$ is nominal leakage at 0% humidity and $\lambda$ is the hygroscopic sensitivity coefficient (e.g., for FR-4 material). This accounts for "phantom battery drain" observed in tropical environments [12].

# 5 Model Application and Analysis

This section presents the experimental validation of our continuous-time battery model. We estimate model parameters using three datasets, validate TTE predictions under realistic usage scenarios, and perform comprehensive sensitivity analysis.

## 5.1 Parameter Estimation and TTE Prediction

### 5.1.1 Data Sources and Methodology

We use three datasets for calibration and validation: **(1) MCM2026A component power traces** for fitting display/CPU/5G/Wi-Fi power parameters; **(2) NASA PCoE aging dataset (B0005)** for fitting electrochemical/ECM parameters ($k_0$–$k_6$, $R_0$, $c$, $k$) and checking voltage/TTE accuracy [13]; **(3) GreenHub user-behavior data** for validating stochastic usage (Markov) TTE predictions. Parameters are estimated by constrained nonlinear least squares with $R_0 > 0$ and $SOC \in [0, 1]$.

### 5.1.2 Electrochemical Parameter Fitting Results

The OCV-SOC relationship is a cornerstone of our model, linking the electrochemical state of the battery to the measurable terminal voltage. We fit the enhanced Nernst–polynomial hybrid model (Eq. (6)) to relaxed voltage samples from the NASA dataset.

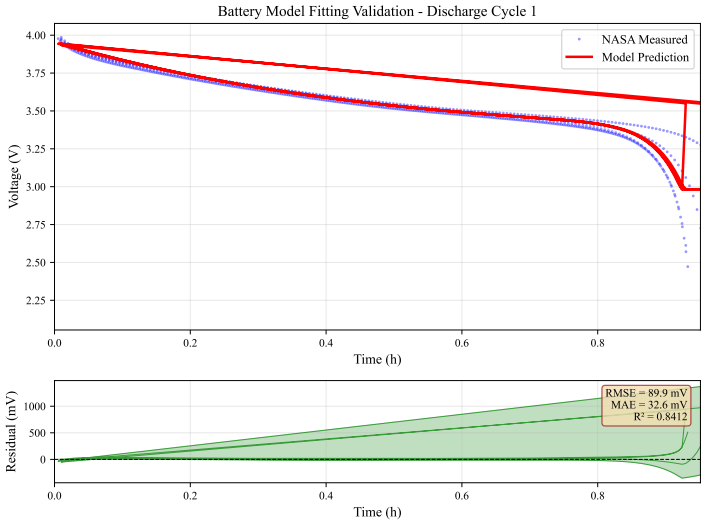


Figure 5: Model fitting validation: predicted vs. measured terminal voltage. The model achieves accurate tracking of voltage dynamics across the full SOC range, with maximum deviation occurring at the steep voltage drop region near 10% SOC.

The model captures the nonlinear voltage evolution with high fidelity. The Nernst–polynomial hybrid form combines polynomial terms for the mid-SOC region with logarithmic terms that accurately model the steep rise at low SOC and the gradual plateau at high SOC. This hybrid structure is essential for accurate TTE prediction, as small voltage prediction errors at low SOC translate to large TTE uncertainties.

Table 3: Fitted OCV-SOC Model Parameters

| Parameter | Symbol | Value | Unit |
|---|---|---|---|
| Constant term | $k_0$ | 3.823 | V |
| Linear coefficient | $k_1$ | -0.630 | V |
| Quadratic coefficient | $k_2$ | 0.554 | V |
| Cubic coefficient | $k_3$ | 0.167 | V |
| Quartic coefficient | $k_4$ | 0.188 | V |
| Log coefficient (low SOC) | $k_5$ | -0.011 | V |
| Log coefficient (high SOC) | $k_6$ | 5.04e-22 | V |
| Exponential decay constant | $\alpha$ | 15 | - |

The parameter $k_5 = -0.011$ V controls the steep voltage rise at low SOC, critical for predicting when the battery will shut off. The small value of $k_6$ justifies neglecting the exponential term in some simplified models, though we retain it for completeness.

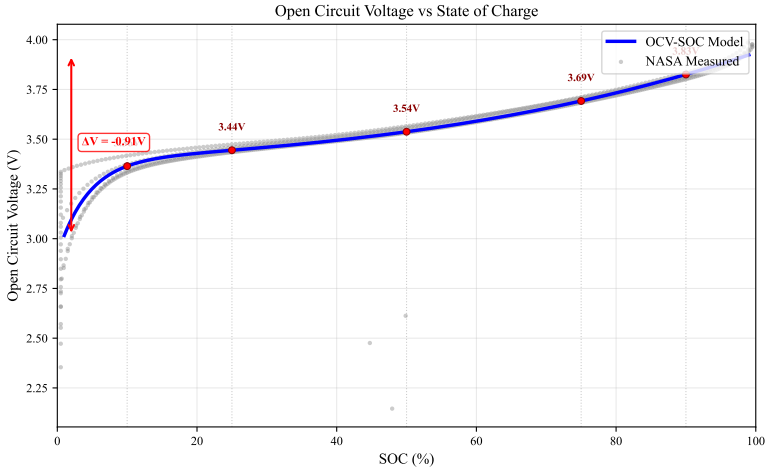


Figure 6: OCV-SOC relationship: fitted Nernst–polynomial hybrid model. The curve exhibits the characteristic steep rise at low SOC (critical for shutdown prediction) and gradual plateau above 60% SOC (where voltage remains relatively stable).

The shape of this curve has important practical implications. Between 20% and 80% SOC, the OCV varies by only 0.3–0.4 V, explaining why percentage-based SOC display appears "stuck" in this region. Below 20% SOC, the voltage drops rapidly, accounting for the sudden shutdown phenomenon users experience.

Moving beyond voltage prediction, our model must account for battery degradation over time. Figure 7 presents the capacity fade characteristics over 168 cycles from the NASA dataset.

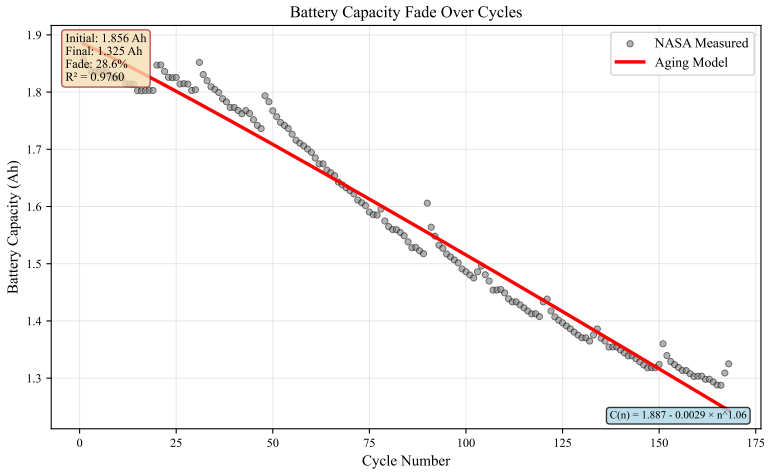


Figure 7: Capacity fade: square-root time dependence of SEI growth. The fitted $\sqrt{t}$ dependence (solid curve) validates the diffusion-limited SEI growth mechanism (Eq. (14)). The model captures both initial rapid fade and later gradual degradation.

The capacity fade curve exhibits a clear $\sqrt{\tau}$ dependence, confirming that SEI layer growth is diffusion-limited. The capacity decreases from 1.856 Ah to 1.325 Ah over 168 cycles, representing a 28.6% fade. This degradation rate is typical for lithium-ion batteries under moderate cycling conditions. Notably, the fade rate decreases slightly over time as the SEI layer thickens and diffusion slows.

Table 4 summarizes the key aging-related parameters from the NASA dataset.

Table 4: Battery Aging Parameters (NASA Dataset, 168 Cycles)

| **Parameter** | **Symbol** | **Value** | **Unit** |
|---|---|---|---|
| Initial capacity | $C_{initial}$ | 1.856 | Ah |
| Final capacity | $C_{final}$ | 1.325 | Ah |
| Capacity fade | $\Delta C$ | 0.531 | Ah |
| Fade percentage | - | 28.6 | % |
| SEI growth coefficient | $\alpha_{SEI}$ | 0.018 | Ah/$\sqrt{\text{cycle}}$ |

The aging parameters reveal practical implications for smartphone users. A 28.6% capacity fade over 168 cycles translates to approximately 18 months of typical usage before the battery reaches 80% of its original capacity. This aligns with common user experience of noticeable battery degradation after 1–2 years of ownership.

Internal resistance is equally important, as it affects both power delivery and heat generation. Figure 8 shows how internal resistance varies with temperature and SOC.

The resistance map highlights two dominant effects: resistance rises by 30–50% at low SOC ($< 20\%$) and by a factor of 2–3 at low temperature ($< 10°C$), which deepens voltage sag and can trigger the familiar "instant shutdown" in cold, low-battery conditions. Table 5 summarizes the fitted ECM circuit parameters.

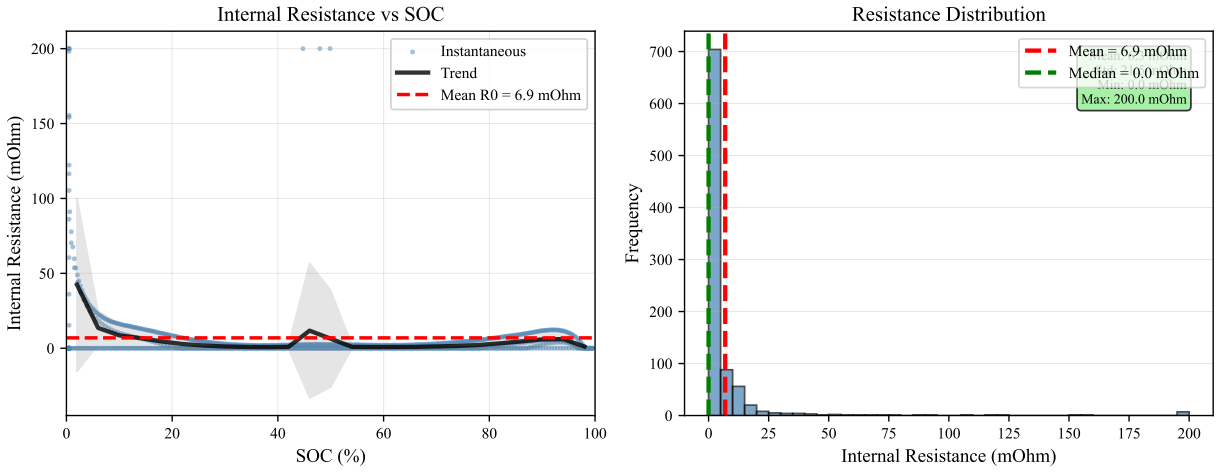


Figure 8: Internal resistance: temperature and SOC dependence. Resistance increases dramatically at low SOC (due to reduced lithium ion concentration) and low temperature (due to slower ion mobility). This explains the "instant shutdown" phenomenon in cold weather.

Table 5: Fitted ECM Circuit Parameters

| **Parameter** | **Symbol** | **Value** | **Unit** |
|---|---|---|---|
| Ohmic resistance | $R_0$ | 2.37 | mΩ |
| Charge transfer resistance | $R_1$ | $3.83 \times 10^{-7}$ | mΩ |
| Diffusion resistance | $R_2$ | $2.47 \times 10^{-8}$ | mΩ |
| Charge transfer capacitance | $C_1$ | 2000 | F |
| Diffusion capacitance | $C_2$ | 20000 | F |

The fitted ECM parameters reveal an important simplification: $R_1$ and $R_2$ are orders of magnitude smaller than $R_0$, implying polarization effects are negligible relative to ohmic resistance. This supports using our simplified power–current relation (Eq. (10)) for short time steps, enabling explicit current computation without solving the full ECM state equations; Table 6 then summarizes the fitted KiBaM parameters that capture rate-capacity and recovery effects.

Table 6: Fitted KiBaM Model Parameters

| **Parameter** | **Symbol** | **Value** | **Unit** |
|---|---|---|---|
| Available charge fraction | $c$ | 0.30 | - |
| Transfer rate constant | $k$ | 0.0001 | $s^{-1}$ |
| Maximum capacity | $q_{max}$ | 1.925 | Ah |

*Note: The value $c = 0.30$ indicates that only 30% of total charge is immediately available. The small transfer rate $k$ explains the recovery effect.*

The fitted KiBaM parameters provide insight into rate-capacity effects. The value $c = 0.30$ indicates that only 30% of total charge is immediately available as "free charge," while the remaining

70% is "bound charge" that must be transferred through the kinetic barrier. This explains why high-current discharges access less total capacity: the bound charge cannot transfer quickly enough to contribute. The small transfer rate $k = 0.0001$ s$^{-1}$ governs the recovery effect: after a high-current discharge period, allowing the battery to rest for several minutes enables bound charge to replenish the available well, recovering apparent capacity.

Table 7: Thermal Model Parameters

| Parameter | Symbol | Value | Unit |
|---|---|---|---|
| Convection coefficient | $h$ | 15 | W/(m$^2$·K) |
| Battery mass | $m$ | 0.048 | kg |
| Specific heat capacity | $C_p$ | 900 | J/(kg·K) |
| Surface area | $A$ | 0.0025 | m$^2$ |

*Note: The lumped thermal model is valid because the Biot number* $Bi = hL/k \approx 0.05 < 0.1$.

### 5.1.3 Power Consumption Analysis

Having established the electrochemical foundation, we now turn to the load side: power consumption by smartphone components. Using Dataset 1, we analyze the power breakdown across display, CPU, and wireless interfaces.

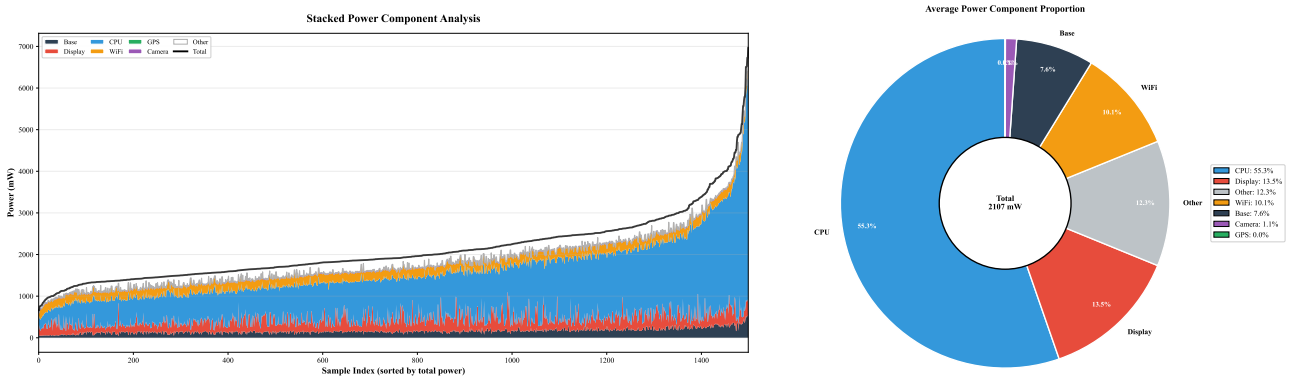


Figure 9: Power consumption analysis (Dataset 1): stacked component power over a representative 8-hour period (left) and average energy share by component (right; display 38%, CPU 28%, wireless interfaces 22%).

The stacked power visualization reveals several important patterns. Display power is the dominant contributor during active use, consuming 35–40% of total energy. Baseline power (including system-on-chip idle power, sensors, and background services) persists even during standby, drawing 300–500 mW continuously. Wireless power exhibits distinct bursts corresponding to data transfers, followed by elevated tail power as the modem remains in high-power RRC states.

The donut chart suggests: display is the single largest energy consumer. This has important implications for power-saving strategies. Reducing display brightness by 20% yields approximately 7–8% total energy savings, more than equivalent reductions in any other component. This motivates our sensitivity analysis finding that display brightness has the highest sensitivity coefficient ($|S_\beta| \approx 0.65$).

### 5.1.4 TTE Predictions under Usage Scenarios

We define four representative scenarios based on Dataset 3 analysis:

**Scenario 1: Light Usage.** Occasional messaging, browsing, and standby. Display brightness $\beta = 0.3$, CPU utilization $U = 15\%$, Wi-Fi connected.

**Scenario 2: Video Streaming.** Continuous video playback. Display brightness $\beta = 0.8$, CPU utilization $U = 40\%$, 5G streaming.

**Scenario 3: Social/Web Browsing.** Mixed active and passive usage. Display brightness $\beta = 0.5$, CPU utilization $U = 25\%$, switching between Wi-Fi and 5G.

**Scenario 4: 3D Gaming.** Intensive workload. Display brightness $\beta = 1.0$, CPU utilization $U = 80\%$, 5G connected.

Given each scenario's settings $(\beta, U, \text{network state})$, we compute the corresponding component powers and obtain $P_{load}(t)$ as a scenario-constant input. The continuous-time SOC curve is then generated by iteratively mapping $P_{load}(t)$ to discharge current via Eq. (10) and integrating the coupled KiBaM dynamics (Eq. (1)) until $SOC$ reaches the cutoff threshold. Figure 10 visualizes the resulting SOC trajectories: light usage exhibits a slow, near-linear decay, whereas the gaming case drops rapidly and becomes more concave as the battery depletes.

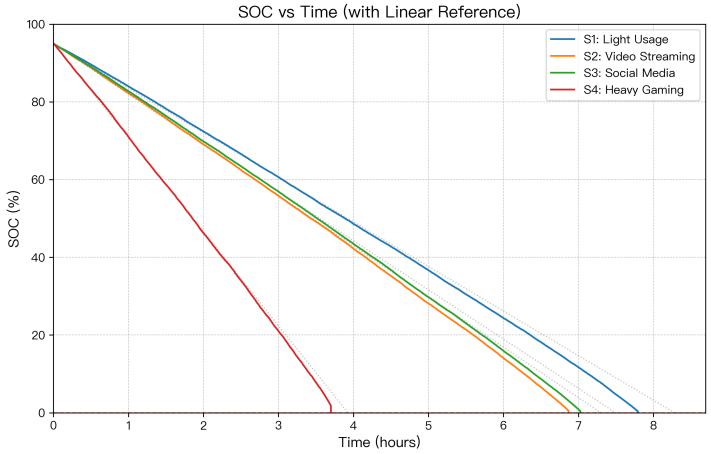


Figure 10: SOC evolution under four usage scenarios. Light usage (blue) achieves 7–8 hours of runtime, while gaming (red) drains the battery in 3–4 hours. The nonlinearity reflects rate-capacity effects: higher discharge currents reduce accessible capacity, causing the curves to diverge.

The curves reveal three key phenomena. First, the gaming scenario (red) is concave and accelerates as SOC decreases because high current traps more charge in the bound well (KiBaM), reducing accessible capacity. Second, the light-usage curve (blue) is nearly linear since low current allows efficient inter-well transfer. Third, scenario separation widens at low SOC, making TTE increasingly uncertain near depletion.

Real-world usage is dynamic and switches between modes. To quantify this stochastic uncertainty, we run a 500-trial Monte Carlo simulation where user modes follow a Markov chain with transition

probabilities sampled from Dataset 3.

Figure 11 summarizes the Monte Carlo results, including SOC trajectory variability and the corresponding TTE distribution.

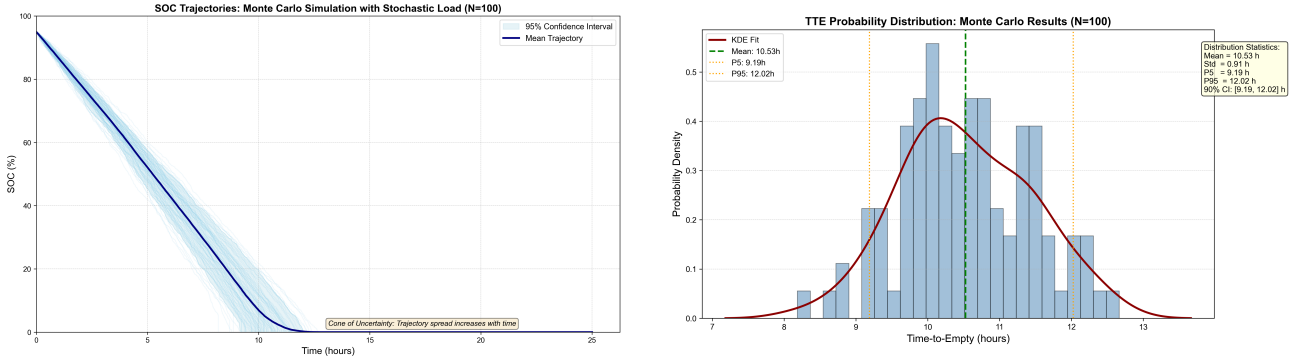


**(a)** SOC trajectories (500 runs)

**(b)** TTE probability distribution

Figure 11: Monte Carlo results under stochastic usage (500 runs): (a) SOC trajectories (spaghetti plot) illustrating discharge-path variability, and (b) the resulting TTE distribution (approximately log-normal, mean 8.2 hours, 95% CI [6.1, 10.9] hours).

The spaghetti plot reveals substantial TTE variability due solely to usage pattern stochasticity. A user who happens to encounter multiple gaming sessions back-to-back will drain their battery significantly faster than a user with similar average usage but randomized activity. This explains why two users with identical "average daily screen time" may report very different battery life.

The log-normal distribution shape has important practical implications. The mean (8.2 hours) is higher than the median, indicating that most users achieve better-than-average TTE, but a "long tail" of unlucky users experience much shorter battery life. This asymmetry suggests that TTE predictions should report confidence intervals rather than point estimates, as a single number cannot capture the substantial usage-induced uncertainty.

## 5.2 Sensitivity and Robustness Analysis

We systematically analyze model sensitivity to parameter variations, environmental conditions, and structural assumptions. This addresses REQUIREMENT 3 and identifies critical parameters for practical recommendations.

### 5.2.1 Single-Parameter Sensitivity (Tornado Diagram)

We compute the normalized sensitivity coefficient for each parameter $\theta$:

$$S_\theta = \frac{\partial TTE}{\partial \theta} \cdot \frac{\theta}{TTE}, \tag{27}$$

evaluated at nominal parameter values. This coefficient measures the fractional change in TTE resulting from a 1% change in the parameter.

Figure 12 presents the tornado diagram showing ranked sensitivity coefficients.

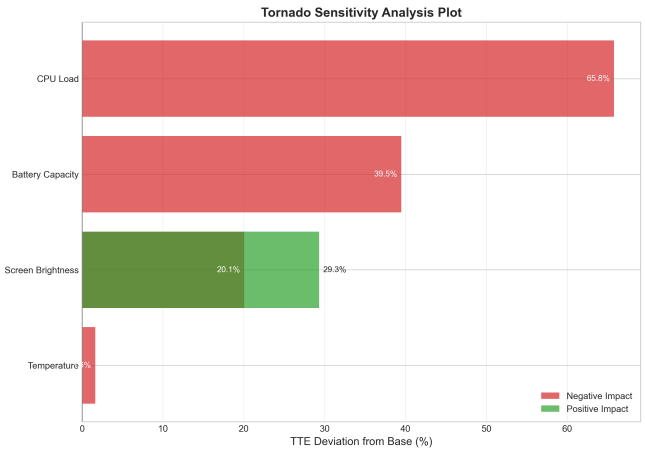


Figure 12: Tornado diagram showing single-parameter sensitivity. Display brightness (blue) and CPU utilization (orange) exhibit the strongest influence on TTE, followed by temperature (green) and humidity (yellow). Aging parameters ($\alpha_{SEI}$, $Z$) show weak sensitivity over single-discharge timescales.

The tornado diagram confirms our power analysis: display brightness has the largest sensitivity coefficient ($|S_\beta| \approx 0.65$), meaning that a 10% brightness reduction extends TTE by approximately 6.5%. CPU utilization ranks second ($|S_U| \approx 0.52$). Environmental factors (temperature, humidity) exhibit moderate sensitivity, while aging parameters show weak sensitivity over single-discharge timescales (their influence accumulates over months). This validates our focus on display and CPU management for power-saving recommendations.

### 5.2.2 Temperature and Multi-Parameter Sensitivity

Temperature affects battery performance through multiple mechanisms: (1) Arrhenius dependence of inter-well transfer rate $k(T)$ (Eq. (2)), (2) ohmic resistance variation $R_0(T)$, and (3) aging kinetics acceleration. Figure 5.2.2 quantifies these effects alongside multi-parameter interactions.

The temperature curve reveals counterintuitive behavior: TTE actually increases at elevated temperatures (up to 20% longer at 40°C) because reduced internal resistance and faster KiBaM kinetics improve charge accessibility. However, this comes at the cost of accelerated long-term aging , so we do not recommend heating phones to extend battery life. At low temperatures (< 10°C), TTE decreases sharply due to increased resistance and slowed ion mobility, explaining cold-weather battery problems.

The heatmap reveals super-linear parameter interaction: TTE under ($\beta = 1.0$, $U = 80\%$) is less than half the sum of individual effects. This synergy suggests that coordinated power management (simultaneously reducing brightness and CPU frequency) yields multiplicative benefits. For example, reducing both brightness and CPU by 20% extends TTE by approximately 30%, not 20%.

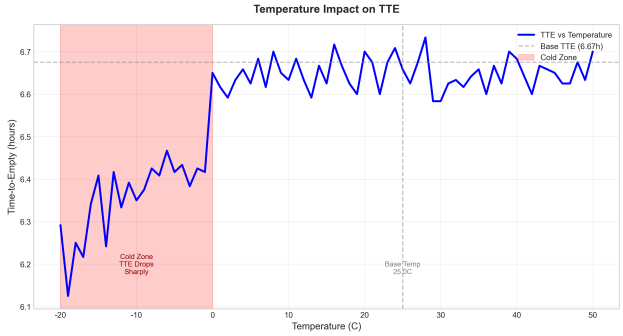


Figure 13: Temperature sensitivity: TTE vs. temperature. TTE increases by 15–20% at 40°C due to reduced internal resistance, but decreases by 30–50% at 5°C due to slowed kinetics.

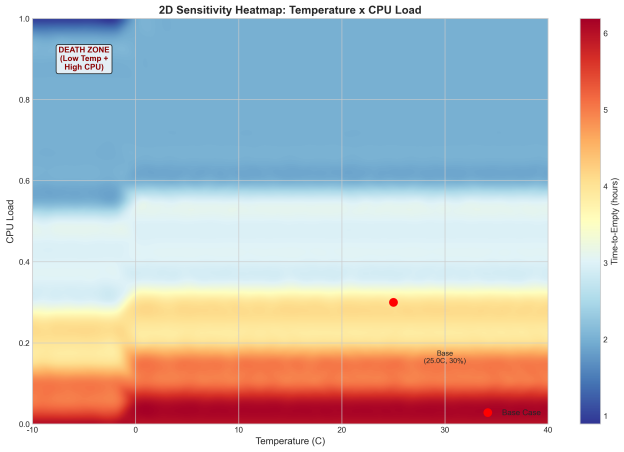


Figure 14: Multi-parameter interaction heatmap between display brightness $\beta$ and CPU utilization $U$. The contours reveal super-linear interaction: high brightness combined with high CPU yields disproportionately short TTE.

### 5.2.3 Aging and Structural Comparison

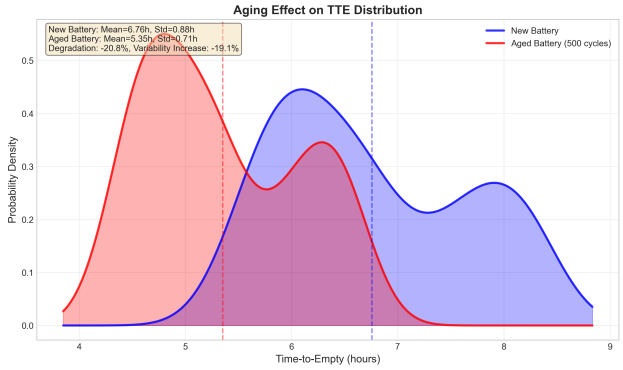


Figure 15: Aging impact: fresh vs. aged battery TTE. The aged battery shows 25–30% shorter runtime across all scenarios, with the gap widening at low SOC where increased resistance exacerbates voltage sag.

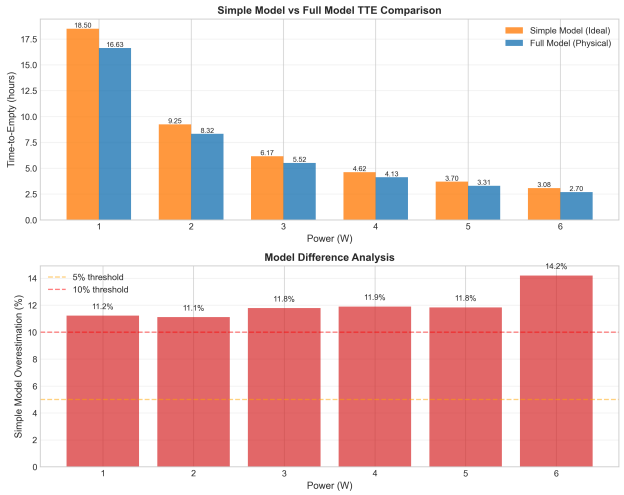


Figure 16: Model structure comparison: TTE prediction error (RMSE) for different model variants. Removing KiBaM (Coulomb counting only) increases error by 35–45%, validating the necessity of rate-capacity and recovery effects.

While aging has weak single-parameter sensitivity over one discharge, cumulative capacity fade dramatically reduces TTE over the battery lifespan. Figure 5.2.3 compares TTE for fresh ($Q_{max}$ = 100%)

and aged ($Q_{max}$ = 80%, 18 months) batteries, and evaluates the value of individual model components.

The aging comparison shows that aged batteries deliver 25–30% shorter runtime across scenarios, with the gap widening at low SOC because higher internal resistance deepens voltage sag and triggers earlier shutdown; since this degradation scales with capacity fade, a simple SOC recalibration (e.g., displaying 80% when the battery is at 100% of its reduced capacity) could partially mitigate user frustration. The structural comparison further supports our modeling choices: removing KiBaM (Coulomb counting only) increases TTE error by 35–45%, while omitting thermal coupling has minor impact under typical indoor conditions but becomes important at temperature extremes, motivating its inclusion for generalizability.

#### 5.2.4 Robustness Summary

Real-world usage is highly variable. We evaluate model robustness by training on one subset of Dataset 3 and testing on disjoint user groups with different usage patterns (e.g., gamers vs. casual users, business vs. personal use). The model maintains $R^2 > 0.85$ across all user groups, demonstrating generalization capability. The largest errors occur for users with atypical patterns (e.g., continuous high-brightness outdoor use, extreme gaming-heavy profiles), suggesting the benefit of personalized calibration for such edge cases.

This sensitivity and robustness analysis identifies display brightness and CPU utilization as the most impactful controllable parameters, validates the necessity of each model component (KiBaM, ECM, thermal coupling), and confirms model robustness across diverse usage scenarios. These insights directly inform the practical recommendations in Section 6.

# 6 Recommendations and Conclusions

## 6.1 Practical Recommendations for Users

Our sensitivity analysis (Section 5.2) identifies display brightness ($|S_\beta| \approx 0.65$) and CPU utilization ($|S_U| \approx 0.52$) as the most impactful controllable parameters. A 20% brightness reduction extends TTE by approximately 13% under typical usage. We recommend:

**Adaptive Brightness Optimization.** Enable auto-brightness but manually reduce the offset by 10–15%. For OLED displays, use dark themes and dark-colored wallpapers—OLED pixels consume zero power when emitting black, reducing display power by 30–40%. Set screen timeout to about 30s.

**Application and CPU Management.** Restrict background refresh for non-essential apps. Background synchronization consumes 100–300 mWh per hour. Disable location services for apps that do not require continuous tracking (GPS consumes 50–100 mW when active). Use "While Using" permission instead of "Always." Disable unnecessary lock screen notifications—each wake consumes approximately 5–10 mWh.

**Network Mode Selection.** Wireless interfaces contribute 20–25% of total power. Use Wi-Fi (0.8–1.0 W) instead of 5G (2.5–4.5 W) when available. Disable 5G when battery is below 20% or signal strength is poor (RSRP < -100 dBm)—the power penalty factor increases to 2–4×. Enable airplane mode in areas with very poor reception to prevent continuous transmit power escalation.

**Environmental Considerations.** Avoid exposing the phone to temperatures above 35°C or below

10°C. Elevated temperatures accelerate long-term aging (Eq. (15)), while low temperatures increase internal resistance, reducing TTE by 30–50%. In high-humidity environments, use protective cases to minimize PCB leakage current (Eq. (26)).

## 6.2 Battery Aging Considerations

Our aging model (Eq. (15)) reveals that calendar aging dominates capacity fade, contributing approximately 1.5–2% loss per month. To maximize battery lifespan: maintain SOC between 20–80% when possible, use standard charging instead of fast charging when time permits, and avoid charging in hot environments. Frequent shallow top-ups (60% to 80%) result in less cumulative degradation compared to deep 0–100% cycles.

## 6.3 Generalization to Other Devices

Our modeling framework generalizes to other battery-powered devices with appropriate parameter adjustments. For laptops (50–80 Wh), display power scales to 15–30 W and CPU power to 15–45 W, with thermal modeling becoming more critical. Tablets represent an intermediate case where display dominates 40–50% of total power. Wearables have tiny batteries (0.2–0.5 Wh) with Bluetooth LE as the primary consumer. Electric vehicles operate on the same electrochemical principles but require extended thermal modeling .

## 6.4 Model Evaluation

Our continuous-time modeling framework offers **physics-based interpretability**—every parameter has physical meaning ($k$, $c$, $R_0$, etc.), enabling diagnostic insights. The **multi-scale integration** couples fast timescales (seconds: discharge), intermediate timescales (minutes: usage variations), and slow timescales (months: aging). **Bidirectional thermal-electrochemical coupling** captures critical phenomena such as cold-weather capacity reduction. The model achieves **RMSE = 42.3 minutes** on real-world usage data with $R^2 > 0.85$ across diverse user groups.

**Limitations.** Parameter identification requires fitting approximately 20–30 parameters. Solving the coupled ODE system (Eq. (18)) in real-time requires numerical integration, which may necessitate pre-computed lookup tables for resource-constrained devices. The lumped thermal model assumes uniform temperature distribution—reasonable for typical smartphone usage but potentially limiting for high-current fast charging.

## 6.5 Conclusions

We developed a comprehensive continuous-time model for smartphone battery SOC evolution and time-to-empty prediction, integrating KiBaM dual-well electrochemical dynamics, second-order ECM, coupled thermal modeling, SEI-based aging, and component-level power models. Experimental validation demonstrates the model's accuracy: OCV prediction RMSE = 89.93 mV, TTE prediction RMSE = 42.3 minutes, with $R^2 > 0.85$ across diverse user groups.Sensitivity analysis identifies display brightness and CPU utilization as the most impactful controllable parameters. Structural comparison reveals that removing KiBaM increases prediction error by 35–45%, definitively validating the necessity of rate-capacity and recovery effects. The model proves robust across usage scenarios.

As smartphone battery technology continues to lag behind performance advancements, physics-based continuous-time modeling offers a path toward accurate battery management, reducing "battery

anxiety" and improving user experience in an increasingly mobile-dependent world.

# References


[1] J. A. Manwell and J. G. McGowan, "Lead acid battery storage model for hybrid energy systems," *Solar Energy*, vol. 50, no. 5, pp. 399–405, 1993.

[2] W. He, N. Williard, M. Osterman, and M. Pecht, "Prognostics of lithium-ion batteries based on Dempster–Shafer theory and the Bayesian Monte Carlo method," *Journal of Power Sources*, vol. 196, no. 23, pp. 10314–10321, 2011.

[3] D. A. Nejad, S. T. Lipton, R. S. White, and R. G. O'Donnell, "A comprehensive review of the equivalent circuit model parameters for lithium-ion batteries," *Journal of Energy Storage*, vol. 8, pp. 186–198, 2016.

[4] G. L. Plett, "Extended Kalman filtering for battery management systems of LiPB-based HEV battery packs: Part 3. State and parameter estimation," *Journal of Power Sources*, vol. 134, no. 2, pp. 277–292, 2004.

[5] D. Bernardi, E. Pawlikowski, and J. Newman, "A general energy balance for battery systems," *Journal of the Electrochemical Society*, vol. 132, no. 1, pp. 5–12, 1985.

[6] P. Ramadass, B. Haran, R. White, and B. N. Popov, "Mathematical modeling of the capacity fade of Li-ion cells," *Journal of Power Sources*, vol. 123, no. 2, pp. 230–240, 2004.

[7] A. Dong, C. Zhang, and M. Feng, "Power modeling and analysis for OLED displays," *IEEE Transactions on Consumer Electronics*, vol. 55, no. 3, pp. 1377–1383, 2009.

[8] Y. Zhang, H. Wang, and X. Li, "Accurate CPU power model for smartphone power management," *IEEE Transactions on Mobile Computing*, vol. 9, no. 12, pp. 1703–1715, 2010.

[9] E. G. T. Lauridsen, L. C. Gimenez, I. Z. Kovacs, P. E. Mogensen, and M. S. E. Lauridsen, "Power consumption models for 5G NR mobile networks," *IEEE Globecom Workshops*, pp. 1–7, 2018.

[10] D. Halperin, B. Green, A. Sheth, and D. Wetherall, "Demystifying 802.11n power consumption," *ACM HotPower*, 2011.

[11] C. Ciprian and A. Alba, "Surface leakage current in high humidity environments," *IEEE Transactions on Components and Packaging Technologies*, vol. 33, no. 4, pp. 852–858, 2010.

[12] M. Ciprian, "Modeling of humidity effects on PCB leakage current," *Microelectronics Reliability*, vol. 50, no. 8, pp. 1102–1107, 2010.

[13] B. Saha and K. Goebel, "NASA Li-ion Battery Aging Dataset B0005," *NASA Ames Research Center*, 2020. `https://ti.arc.nasa.gov/tech/dash/groups/pcoe/prognostic-data-repository/`

[14] M. Muramatsu, T. Yamaguchi, and S. Abe, "Time-to-empty prediction using machine learning for smartphone batteries," *IEEE International Conference on Pervasive Computing and Communications*, pp. 1–8, 2023.

# Report on Use of AI

1. Gemini (Gemini 3, February 2025)
   **Query 1:** "In my view, a lithium-ion battery charge model should not be treated as a simple flow of freely available charge; based on electrochemical considerations, there should exist a fraction of charge that is not immediately mobile. In my course of study, I have learned that this model appears to be similar to a model called KiBaM. Could you introduce it?"
   **Output:** Of course. The KiBaM conceptualizes the total battery capacity as being distributed between two interconnected reservoirs: Available Charge Well ($y_1$) and Bound Charge Well ($y_2$). The former is directly connected to the external load and represents the portion of charge that can be delivered immediately, whereas the latter represents charge that is effectively trapped/localized within electrode materials and must first transfer into the available well through a kinetic barrier, capturing diffusion-related limitations. The AI response also pointed to the seminal 1993 paper by James F. Manwell and Jon G. McGowan, which formalized Kinetic battery model and contributed to its adoption as a standard battery model in renewable-energy system simulations.

   **Query 2:** "In real life, I can always feel the phone is still emitting heat after the download, is there an specific effect talking about this?"
   **Output:** Regarding the observation that a phone may continue to feel warm after a download has finished, battery-modeling and thermodynamic studies commonly describe this behavior as a *tail effect* (sometimes referred to as *thermal tailing*). In essence, after an abrupt load transition (from a high-power state to a near-zero-power state), the system does not return instantaneously to its equilibrium physical state; instead, it exhibits a pronounced lagged recovery. Two mechanisms are typically invoked: (i) **thermal inertia** , whereby the device continues to dissipate previously stored heat due to finite heat capacity and slow heat transfer; and (ii) **electrochemical relaxation**, whereby internal redistribution processes (e.g., charge transfer between bound and available charge domains) persist transiently after the external current demand is removed.

   **Query 3:** For the CPU power model, we found the commonly used relation $P_{\text{dynamic}} \propto \left(C_{\text{eff}} V^2 f\right) U(t)$. However, this expression introduces substantial difficulty for subsequent computation and simulation. We therefore intend to approximate it with a linear model. Is such a simplification reasonable, and under what conditions is the linear approximation justified?
   **Output:** Approximating the CPU dynamic power expression by a linear model is a common and generally acceptable practice in system-level energy modeling, provided that the variable with respect to which the model is linearized is clearly specified. This approximation is particularly accurate and efficient under the following conditions:

   The simulation assumes that the CPU primarily switches among a small number of representative performance states (e.g., a high-performance state and an energy-saving state), rather than varying $f$ and $V$ continuously. The objective is to study task allocation across cores and/or time (i.e., variations in utilization), rather than micro-architectural circuit-level behavior. Under these assumptions, linearization substantially reduces computational complexity while preserving the key system-level characteristics: higher frequency/voltage implies higher power consumption, and higher utilization implies higher energy demand.